Fe-K line probing of material around the AGN central engine with Suzaku

Yasushi Fukazawa[1], Kazuyoshi Hiragi[1], Motohiro Mizuno[1], Sho Nishino[1], Katsuhiro Hayashi[1], Tomonori Yamasaki[1], Hirohisa Shirai[1], Hiromitsu Takahashi[1]

Department of Physical Science, Hiroshima University, 1-3-1 Kagamiyama, Higashi-Hiroshima, Hiroshima 739-8526, Japan

fukazawa@hep01.hepl.hiroshima-u.ac.jp

and

Masanori Ohno[2]

Institute of Space and Astronautical Science (ISAS), Japan Aerospace Exploration Agency (JAXA), 3-1-1 Yoshinodai, Chuo-ku Sagamihara, Kanagawa 252-5120, Japan

ABSTRACT

We systematically analyzed the high-quality Suzaku data of 88 Seyfert galaxies, about 31% of which are Compton-thick AGNs. We obtained a clear relation between the absorption column density and the equivalent width (EW) of the 6.4 keV line above 10^{23} cm^{-2}, suggesting a wide-ranging column density of $10^{23-24.5}$ cm^{-2} with a similar solid and a Fe abundance of 0.7–1.3 solar for Seyfert 2 galaxies. The EW of the 6.4 keV line for Seyfert 1 galaxies are typically 40–120 eV, suggesting the existence of Compton-thick matter like the torus with a column density of $> 10^{23}$ cm^{-2} and a solid angle of $(0.15 - 0.4) \times 4\pi$, and no difference of neutral matter is visible between Seyfert 1 and 2 galaxies. An absorber with a lower column density of 10^{21-23} cm^{-2} for Compton-thin Seyfert 2 galaxies is suggested to be not a torus but an interstellar medium. These constraints can be understood by the fact that the 6.4 keV line intensity ratio against the 10–50 keV flux is almost identical within a range of 2–3 in many Seyfert galaxies. Interestingly, objects exist with a low EW, 10–30 eV, of the 6.4 keV line, suggesting that those torus subtends only a small solid angle of $< 0.2 \times 4\pi$. Thanks to high quality data with a good signal-to-noise ratio and the accurate continuum determination of Suzaku, ionized Fe-Kα emission or absorption lines are detected from several percents of AGNs. Considering the ionization state and equivalent width, emitters and absorbers of ionized Fe-K lines can be explained by the same origin, and highly ionized matter is located at the broad line region. The rapid increase

in EW of the ionized Fe-K emission lines at $N_{\rm H} > 10^{23}$ cm^{-2} indicates that the column density of the ionized material also increases together with that of the cold material. It is found that these features seem to change for brighter objects with more than several 10^{44} erg s^{-1} such that the Fe-K line features become weak. This extends the previously known X-ray Baldwin effect on the neutral Fe-Kα line to ionized emission or absorption lines. The luminosity-dependence of these properties, regardless of the scatter of black hole mass by two orders of magnitudes, indicates that the ionized material is associated with the structure of the parent galaxy rather than the outflow from the nucleus.

Subject headings: galaxies: active — galaxies: Seyfert — X-rays: galaxies

1. Introduction

X-ray spectra from Seyfert galaxies are never represented by a simple power-law, but a wide range of reprocessed features such as absorption, emission and absorption lines, reflection, and so on (Turner and Miller 2009). Such features are vital to probe the surrounding material around central supermassive black holes, such as accretion disk or flow, torus, and clouds. Since such materials are fuel for massive black holes, information on the evolution of the supermassive black holes can be obtained by studying them.

The most prominent feature is the photoelectric absorption of the continuum in the soft X-ray band, where both cold and warm absorbers are found. The cold matter is thought to be associated with a molecular torus. For Compton-thin objects with a cold absorption column density of $N_{\rm H} < 10^{23}$ cm^{-2}, $N_{\rm H}$ can be determined by observations below 10 keV. Based on the observations with BeppoSAX, Swift/BAT, and INTEGRAL, a significant fraction of Seyfert galaxies exhibit a Compton-thick cold absorption (Risaliti et al. 1999; Beckmann et al. 2006; Tueller et al. 2008), and the direct nuclear X-ray emission of such objects cannot be observed below 10 keV. The location and geometry of the cold absorber is now extensively studied. Matt (2000) pointed out that the Compton-thin absorber differs from the Compton-thick molecular torus and is associated with the interstellar medium in the parent galaxy. The rapid time variation of the absorption column density indicates that some of the cold absorbers exist as a blob-like cloud (e.g. Elvis et al. 2004). Compton-thick Seyfert 2 galaxies also exhibit a complex absorption feature, possibly due to partial covering and so on (Comastri et al. 2010). Some of the Compton-thick objects exhibit no optical activity and weak scattering X-ray component, indicating that the torus is geometrically thicker than ever thought (Ueda et al. 2007). A warm absorber due to ionized clouds has often emerged. Although initially recognized through an ionized absorption edge in the soft

X-ray band (Halpern 1984), a lower-density absorber has also recently emerged via detection of soft X-ray and UV absorption lines (e.g. Kaspi et al. 2002). These absorption materials are also observed as reflectors or scatterers, and many emission lines in the optical to X-ray band are detected from Seyfert galaxies (e.g. Kaspi et al. 2002), as are wide-ranging ionization states; for example, the ionization state of iron ranges from 0 to 26.

These materials are considered to be related to the evolution of the central black hole and engine. A recent X-ray survey revealed that heavily absorbed AGNs lack high luminosity (e.g. Ueda et al. 2003; Winter et al. 2009), while blue-shifted absorption lines sometimes emerge in high luminosity AGNs (Pounds et al. 2003; Reeves et al. 2003), indicating a relativistic massive outflow, which is promising feedback for the parent galaxy evolution. With this in mind, it is important to obtain a general view of materials around the supermassive black hole to understand the coevolution of the black hole and galaxy. The physical properties of environmental materials are subject to the luminosity of the central engine. It is also important to understand the complex X-ray spectra of Seyfert galaxies and derive the intrinsic spectral shape, to clarify the physical view of the central engine, while correct modeling of the X-ray continuum emission is also required to evaluate the disk line and the reflection component.

However, the absorption column density and intrinsic luminosity of Compton-thick Seyfert galaxies cannot be measured below 10 keV. In addition, reflection component constraint requires wide X-ray band spectroscopy. BeppoSAX and/or XMM-Newton has provided opportunities for such studies, but the energy resolution of BeppoSAX around Fe-K lines is too poor to resolve the broad/narrow, neutral/ionized, or absorption lines respectively. The variability of Seyfert galaxies means broadband X-ray spectral shapes cannot be ensured when observations below and above 10 keV are not simultaneous. However, the Suzaku XIS/HXD combination (Mitsuda et al. 2007; Koyama et al. 2007; Takahashi et al. 2007; Kokubun et al. 2007) is relatively powerful for such studies, thanks to its wide X-ray band, good energy resolution, and well-calibrated response. Since the typical exposure time of AGNs with Suzaku is longer than 50 ks, the signal-to-noise ratio of data is very high. Here, we report systematic studies of the Fe-K line features of Seyfert galaxies and their dependence on intrinsic luminosity and the cold absorber. We evaluated the Fe line features as free from the modeling as possible to avoid the model dependence of physical quantities, such as solid angles and Fe abundance. The disk line was not treated in this paper, since it depends on continuum modeling.

Throughout this paper, we adopt a Hubble constant of H_0 =70 km s^{-1} Mpc^{-1}. The solar abundance ratio is referred to as the solar photospheric values of Anders and Grevesse (1989) for photoelectric absorption and reflection, and the cross-section for the absorption

model is set to that of Bałucińska-Church and McCammon (1992). The errors are typically shown at a 1σ confidence level for one interesting parameter.

2. Data Sample

We selected Seyfert galaxies from the archived Suzaku data as of September 2009. Initially, we examine XIS and HXD spectra, whereupon the objects detected with HXD-PIN were chosen. The HXD-PIN detection is important to constrain the Compton-thick absorption column density and measure the intrinsic luminosity free from absorption. This condition leads to the selection of objects which are bright enough to analyze the Fe-K line feature with a good signal-to-noise ratio. Consequently, we analyzed 88 objects, about 36% of which were Seyfert 1 galaxies ($N_{\rm H} < 10^{22}$ cm^{-2}), about 33% Compton-thin Seyfert 2 galaxies (10^{22} cm$^{-2} < N_{\rm H} < 5\times10^{23}$ cm^{-2}), and about 31% Compton-thick Seyfert 2 galaxies ($N_{\rm H} >= 5 \times 10^{23}$ cm^{-2}). All the objects were observed in XIS 5x5 or 3x3 modes and normal HXD mode. We screened the data with Suzaku standard selection criteria and the XIS photons accumulated within 4 arcmin of the object, with the XIS- 0, 2, and 3 data coadded to derive the spectrum. The XIS rmf and arf files were created with `xisrmfgen` and `xisarfgen` (Ishisaki et al. 2008), respectively, and the XIS detector background was estimated with `xisnxbgen` (Tawa et al. 2008). For the HXD, the "tuned" PIN and GSO background was used (Fukazawa et al. 2009) and the good time interval (GTi) was determined by taking the logical-and of GTIs among XIS data, HXD data, and HXD background data. For the XIS and HXD-PIN, CXB was added to the background spectrum thus obtained, although negligible for the HXD-GSO. The GSO response correction file *ae_hxd_gsoxinom_20070424.arf* was also utilized, which compensated for any disparity of 10–20% between the Crab spectral model and the data for the current response matrix (Takahashi et al. 2008). In the simultaneous spectral fitting of XIS and HXD, a constant factor of 1.13 was introduced for both PIN and GSO against the XIS.

3. Analysis of the Fe-K line features

In order to study the Fe-K line features, we initially determined the baseline continuum model. Since the Suzaku spectra of most Seyfert galaxies cannot be expressed by a simple power-law model plus absorption, we added a reflection component and an Fe-K line and fitted the spectra above the 3 keV (model A). We applied the *pexrav* model (Zdziarski et al. 1995) for the reflection component. We include both the Galactic and object-intrinsic absorptions. The former was fixed to the value in Dickey & Lockman (1990). For the latter,

the column density and Fe abundance were left free and other elemental abundances were fixed to 1 solar. For the reflection component, Fe abundance and reflection fraction R were left free, but the Fe abundance was tied to that of the absorption. The parameters of the input power-law emission for the pexrav model were fixed to that of the above power-law model, and the inclination θ to $\cos\theta = 0.207$. θ was related to the relative intensity of the reflection component, alongside R. Since the latter was a free parameter, the fixing of θ did not significantly affect the results on continuum modeling. After obtaining these spectral parameters, we restricted the energy band to the range 5–9 keV, and fixed the absorption, reflection fraction, and powerlaw photon index, where the powerlaw normalization was the single free parameter for the continuum model. We included five Gaussians (model B), considering lines of 6.4 keV, 6.7 keV (He-like), 7.0 keV (H-like), and 7.09 keV (neutral Fe-Kβ). Although the line energy and width of 6.4 keV were let free. the center energy of other lines was fixed to the value in the rest frame, and their line width was 0 keV. while a negative value was allowed for the normalization of ionized Fe-K lines; 6.7 and 7.0 keV. The intensity of the Fe-Kβ line was fixed to 0.125 of the Fe-Kα intensity (Palmeri et al .2003), since it is usually too weak to measure accurately in most cases. We do not consider a disk-line, since the disk-line feature could affect the continuum modeling, leading to the systematic uncertainty of the equivalent width. However, since its shape resembles that of the reflection continuum, we believe that the affection is reduced by including the *pexrav* model even if the disk-line exists.

Apart from the line studies, we also obtained the absorption column density for discussion. Although the soft X-ray band could not be reproduced well by a simple model, we fit the spectra with a single power-law model plus Gaussian, multiplied by the absorption and differing from model A in that the metal abundances of all elements were fixed to 1 solar (model C). The energy band for fitting was limited to higher energy than for model A so that complex spectral features in the soft X-ray band could be neglected. Recently, it was revealed that the absorption feature of Seyfert galaxies is more complex than is represented by the single column density (e.g. Comastri et al. 2010), meaning that the column density obtained in this fitting is a typical or representative value for each object. Since we excluded the soft X-ray band, the complex absorption feature in the soft X-ray band did not affect the results for the Fe-K line intensities and the flux in 10-50 keV.

Finally, in order to obtain the Fe-K edge properties, we added the edge model into model B. Since the reflection and absorption include a Fe-K edge feature, the Fe abundance of these components was fixed to 0 solar and other elemental abundances to 1 solar, respectively. We derived the edge energy by allowing the edge energy and depth to be free. To obtain the edge depth τ, the edge energy was fixed to 7.112 keV (X-ray Transition Energy Database `http://www.nist.gov/physlab/data/xraytrans/index.cfm`).

In table 1, we summarize the fitting results for Fe-K line features, together with the absorption column density, X-ray flux, and luminosity in 10–50 keV where the absorption less affects the observed flux: for example, the observed flux is a maximum of 1.5 times as small as the absorption-corrected one in the case of $N_{\rm H} = 2.5 \times 10^{24}$ cm^{-2} with 1 solar abundance. Figure 1 shows a sample of XIS spectra around the Fe-K line features, where only the best-fit continuum model is shown for comparison.

4. Results of the Fe-K Line Features

4.1. Neutral Fe-K Lines and Edge

Figure 2 shows the plots of center energy and width for the 6.4 keV line. Objects with well-determined values reveal center energy within 6.37–6.42 keV and average and variance of 6.399 and 0.008 keV, respectively. Although the uncertainty of the XIS energy scale is 0.01–0.03 keV at 6 keV, the average center energy of the 6.4 keV line is consistent with a neutral or low-ionized Fe-K fluorescence line, which constrains the ionization state to < 12 (Kallman et al. 2004). The line energy is not dependent on the absorption column density; the average and variance are 6.390 and 0.017 keV for $N_{\rm H} < 5 \times 10^{21}$ cm^{-2}, 6.397 and 0.009 keV for $5 \times 10^{21} < N_{\rm H} < 1 \times 10^{23}$ cm^{-2}, and 6.400 and 0.014 keV for $N_{\rm H} > 1 \times 10^{23}$ cm^{-2}, respectively. The width is constrained to be < 3300 km s^{-1} or < 70 eV for objects with well-determined values, and also independent of the absorption column density; the average and variance are 55 and 25 eV for $N_{\rm H} < 1 \times 10^{22}$ cm^{-2}, and 38 and 26 eV for $N_{\rm H} > 1 \times 10^{22}$ cm^{-2}. These constraints are almost similar to those derived for certain individual objects (e.g. Yaqoob et al. 2007; Shirai et al. 2008; Awaki et al. 2008), but the results confirm this as a common feature.

Figure 3 plots an equivalent width (EW) of the 6.4 keV line against the absorption column density. Thanks to effective absorption column density constraints by the HXD data, the clearest ever correlation was obtained (e.g. Guainazzi et al. 2005), between the EW and absorption; a positive correlation above $N_{\rm H} = 10^{23}$ cm^{-2}, and an almost constant EW around 50–120 eV below $N_{\rm H} = 10^{23}$ cm^{-2}. The EW distribution for Compton-thin objects are in good agreement with that of XMM-Newton (Bianchi et al. 2009). The positive correlation is also in good agreement with the prediction of the fluorescence line by the Compton-thick torus with various column density (e.g. Awaki et al. 1991; Ikeda et al. 2009). Note that a clear correlation within the range $N_{\rm H} = (0.4-1) \times 10^{24}$ cm^{-2} is seen and the EW is 400–700 eV at $N_{\rm H} = 10^{24}$ cm^{-2}. Since a typical torus structure with $N_{\rm H} = 10^{24}$ cm^{-2} and 1 solar Fe abundance causes EW of 600–700 eV for the 6.4 keV line (Awaki et al. 1991; Ghisellini et al. 1994; Ikeda et al. 2009), the Fe abundance of the reflector or absorber is considered to

be 0.7–1.3 solar.

When estimating the $N_{\rm H}$ by fitting the spectra with the model C, we fixed the Fe abundance to 1 solar. However, if we set the Fe abundance to 2 or 0.5 solar, the $N_{\rm H}$ systematically changes by a factor of up to 0.83 or 1.03, respectively. Considering that the relation between $N_{\rm H}$ and EW is almost linear around $N_{\rm H} = (0.4 - 1) \times 10^{24}$ cm^{-2} (Ghisellini et al. 1994; Ikeda et al. 2009), the abundance ratio of Fe to other heavy metals, such as O, Ne, Si, and S, is indicated to be close to 0.7–1.3 solar. Figure 5 shows an Fe abundance of the absorber and reflector obtained by fitting the spectra with the model A. In this case, the Fe abundance is determined by the relative strength of the Fe-K edge and the reflection hump around 20 keV, as demonstrated by Reeves et al. (2007). The Fe abundance is well determined to be 0.8–1.5 solar for mildly Compton-thick objects with the average and variance 1.18 and 0.21 solar, respectively, for objects with $10^{23} < N_{\rm H} < 10^{24}$ cm^{-2}. This value is consistent with the estimation from the relation between the Fe-K line EW and $N_{\rm H}$.

However, several objects deviate from this clear relation. Swift J0601,9-8636, NGC 2273, and NGC 4968 show a very large EW of > 1 keV for $N_{\rm H} < 9 \times 10^{23}$ cm^{-2}. Swift J0601,9-8636 is that reported in Ueda et al. (2007), who suggested that this AGN is more buried in the geometrically thick torus than is typical, whereupon a large solid angle of the torus would enhance the Fe line. Awaki et al. (2009) reported that the Suzaku spectrum of NGC 2273 contains a significant fraction of the reflection component around the 6.4 line and their sophisticated spectral modeling reveals a higher $N_{\rm H}$ of $(1.1 - 1.7) \times 10^{24}$ cm^{-2}. meaning that the $N_{\rm H}$ obtained by simple modeling might be underestimated. This situation also applies for NGC 4968, the spectrum of which resembles that of NGC 2273. Some Seyfert 1 AGNs with $N_{\rm H} < 10^{21}$ cm^{-2} show a relatively large EW of ~ 200 eV, but this is due to the time variability of the continuum level; good examples of which are NGC 3227 and NGC 5548 which were observed with Suzaku several times and with the largest EW in the faintest continuum level. Note that no objects exist for which the 6.4 keV line intensity varied among several Suzaku observations (table 1).

On the other hand, certain objects exist with a negligible EW of the 6.4 keV line. The upper limits of EW in table 1 are obtained by fixing the center energy and width to 6.4 keV and 30 eV, respectively. High X-ray luminosity objects exhibit a smaller EW of mostly < 80 eV, and some in particular as low as < 25 eV (IGR J21247+5058, 1H 0419-577, 3C 273, ARK 564, PDS 456, TON_S180). This trend of the Baldwin effect (Iwasawa and Taniguchi 1993) is clearly seen in figure 4, and Suzaku also found a clear trend for the first time even for Seyfert 2 galaxies by accurately measuring the luminosity of the direct component above 10 keV. Note that the sample used contains broad line radio galaxies (3C 120, 3C 390.3, 3C 445, 3C 382, 3C 33, 3C 452, 3C 104) with an X-ray luminosity of $> 10^{44}$ erg s^{-1} (10–50 keV).

Apart from the high luminosity objects, low luminosity objects with luminosity of $< 10^{41}$ erg s^{-1} also show a low EW, such as M 81 and M 106 (Yamada et al. 2009). These objects with a high or low luminosity are considered to have a reflector with a smaller solid angle from the central engine by a factor of > 2 than typical Seyfert galaxies. Except for the above specific situations, there are no extraordinary objects, deviating from the clear EW-$N_{\rm H}$ relation.

An Fe-K edge feature around 7.15 keV reveals additional information about the neutral iron, together with the 6.4 keV line. The edge energy is more sensitive to the ionization state than the fluorescence line energy (Makishima 1986; Kallman et al. 2004), and the observed energy is plotted against the edge depth τ in figure 6 for objects with small error bars, which reveals observed edge energy of around 7.2±0.1 keV and an indicated ionization state of < 9. Limited to $\tau > 0.4$, the edge energy is determined to be below 7.2 keV, tightly constraining the ionization state to < 6 for Compton thicker objects. Note that there is a hint of a higher edge energy for lower τ objects. The average edge energy is 7.204±0.022 and 7.110±0.033 keV for objects with $\tau < 0.3$ and > 0.4, respectively. The energy of the Compton-thicker objects is consistent with that for the neutral Fe-K edge of 7.112 keV (X-ray Transition Energy Database), while the energy of Seyfert 1 galaxies indicates the weak ionization state of 3–7 or the contribution of the disk/absorption line.

Line EW and edge depth τ should suggest a linear correlation if the absorber and reflector have the same column density, ionization degree, and iron abundance, following $\tau \sim \frac{N}{4.2\times10^{23}{\rm cm}^{-2}}$. Figure 7 shows the plot between an edge depth and a 6.4 keV line EW. Both values correlate relatively well, indicating identical origin, while some outliers exist at an edge depth of 0.2–0.5 and a high EW of > 400 eV. These objects are almost Compton-thick (such as NGC 4945), the spectrum of which is dominated by the reflection component. Therefore, the deviation is due to the fact that for these objects, the edge is mainly caused by reflection, whereas for other Compton-thinner objects, it is mainly caused by absorption. The τ scatter for low EW objects is due to the origin of the absorption differing from that of the reflection as described in the discussion. Another possibility is being affected by a disk line or weak unresolved lines around their shallow edge structure.

4.2. Ionized Fe-K Emission and Absorption Lines

Thanks to the unprecedented signal-to-noise ratio of the Suzaku data for many AGNs, it is revealed that ionized emission and absorption lines with equivalent widths of 5–60 and 5–40 eV, respectively, are very common for Seyfert galaxies, regardless of whether type 1 or 2 objects. This is in good agreement with the results for Compton-thin objects, based on the XMM-Newton data (Bianchi et al. 2009). Figure 8 shows the relation of EWs between

6.7 and 7.0 keV lines. Here, although the line intensities correlate well with each other, some deviating objects do exist – some objects showing either a 6.7 keV emission line or a 7.0 keV absorption line (MRK 766, NGC 7582). SWIFT J1628.1+514 shows a 6.7 keV absorption line and a 7.0 keV emission line. The strongest emission lines are seen for Compton-thick Seyfert 2 galaxies (NGC 1068, NGC 4945, MRK 273, CIRCINUS GALAXY, and IRAS 19254-7245). For NGC 1068 and NGC 4945, the 6.7 keV line is strong but the 7.0 keV line less so. Conversely, relatively strong absorption lines are seen for NGC 1365, whose EWs of 6.7 and 7.0 keV absorption lines are around 100 eV. In contrast with the 6.4 keV line, NGC 3227, NGC 5548, and MRK 766 show a variability of ionized Fe-K lines, in such a way that the absorption line at 6.7 keV appeared with increasing flux over a time scale of ~ 10 days. Such variability also emerged for NGC 3783 by XMM-Newton (Reeves et al. 2004).

Figure 9 shows a plot of an equivalent width of 6.7 and 7.0 keV lines against an absorption column density of cold material. Seyfert 1 galaxies show a smaller EW of < 20 eV for both emission and absorption lines, while Compton-thick objects show a large EW for the emission lines; sometimes > 100 eV, with the trend for the emission line resembling that of the 6.4 keV line; the EW is almost constant below $N_{\rm H} = 10^{23}$ cm^{-2} but increases rapidly above $N_{\rm H} = 10^{23}$ cm^{-2}, indicating that the geometrical distribution of highly ionized material is similar to that of the neutral one but the covering solid angle is around 10% of the cold material. This trend is not seen for the absorption line, but a relatively large EW tends to be observed for objects with larger $N_{\rm H}$.

Figure 10 shows a plot of an equivalent width of 6.7 and 7.0 keV lines against an X-ray luminosity (10–50 keV). There is a trend of smaller equivalent width for higher X-ray luminosity. An average of the absolute value of EW, which is taken for objects whose line is significant at 1.5σ level as shown in table 1, is 22 and 11 eV below and above $L_X = 5 \times 10^{43}$ erg s^{-1}, respectively, for the 6.7 keV line. The average for the 7.0 keV line is 24 and 10 eV below and above $L_X = 5 \times 10^{43}$ erg s^{-1}, respectively. Correlation coefficients are calculated at -0.37 and -0.43 for the 6.7 and 7.0 keV lines, respectively, in comparison with -0.39 for the 6.4 keV line. Therefore, the coefficients are almost comparable to that of the 6.4 keV line which shows a clear Baldwin effect, despite the significant errors of the 6.7 and 7.0 keV lines. This is the first hint of the Baldwin effect for ionized Fe-K lines. These correlations suggest that the physical properties of the ionized material are related with the neutral material and the nuclear luminosity.

5. Discussion

5.1. Properties of the Neutral Material Emitting 6.4 keV line

Tne center energy of the 6.4 keV line and the Fe-K edge strongly constrain the ionization states of the absorber/reflector to less than 12 and 6, respectively. This is the most severe constraint to date, thanks to the Suzaku capability. The latter corresponds to the ionization parameter of $\xi = \frac{L}{nR^2} \leq 0.1$, where L is the luminosity of the central engine, n the matter density, and R the distance to the matter (Kallman et al. 2004). The width of the 6.4 keV line is constrained to < 3300 km s^{-1} or <70 eV for objects with well-determined values, suggesting that the origin of the 6.4 keV line is a broad-line region or a torus. The line equivalent width and the edge depth correlate well with each other, indicating that both features are due to the same origin. Therefore, considering the above constraint of ξ and the column density $N_{\rm H} < nR$, the 6.4 keV line likely comes from the neutral matter at $> 3L_{43}N_{\rm H,25}^{-1}$ pc away from the nucleus, where L_{43} and $N_{\rm H,25}$ represent the luminosity and column density in units of 10^{43} erg s^{-1} and 10^{25} cm^{-2}, respectively. The reduced time variability of the 6.4 keV line is also consistent with this picture. Since the inner torus radius is reported at $0.03L_{43}^{0.5}$ pc (Suganuma et al. 2006), the reflection matter is not the outer disk but the torus. The absorption column density reportedly varied rapidly within one day (e.g. Elvis et al .2004) or several weeks (Risaliti et al. 2005). Although the blob-like structures of the Compton-thick absorber could cause such short-term variability, the phenomena could also be attributable to the underlying reflection component, even if only the direct nuclear component varies. Therefore, the fast time variability of the absorption column density must be focused on by carefully considering the reflection component.

Seyfert 1 galaxies and Compton-thin Seyfert 2 galaxies with $N < 10^{23}$ cm^{-2} show a similar EW of 50–120 eV for the 6.4 keV line, regardless of the absorption column density. By simple estimation, a reflection component has an EW of $\sim$1000 eV for 1 solar abundance, $N < 5 \times 10^{23}$ cm^{-2}, and the input powerlaw photon index of 2. Considering the transmission and reflection efficiency of the reflector with a solid angle of Ω and a column density of $N_{\rm H}$, the sum of the direct and reflection components reveals an Fe-K EW of $\sim 300 \frac{\Omega}{4\pi} \frac{N_{\rm H}}{4\times10^{23}{\rm cm}^{-2}}$ eV. Therefore, a Compton-thin absorber cannot create the observed large EW of 50–120 eV, and the Compton-thick reflector with $N_{\rm H} > 10^{23}$ cm^{-2} should exist around the nucleus at the off line of sight even for Seyfert 1 galaxies, with possible candidates including accretion disk or dust torus (Awaki et al. 1991; Guainazzi et al. 2005). Since the constraint of the ionization state of reflectors requires the location of $> 3L_{43}N_{\rm H,25}^{-1}$ pc from the nucleus, the reflector for Seyfert 1 galaxies is not the disk but the torus. The EW of 50–120 eV indicates a solid angle of $(0.2 - 0.7) \times 4\pi$ for the Compton-thick torus with $N_{\rm H} > 4 \times 10^{23}$ cm^{-2} (Ghisellini et al. 1994; Ikeda et al. 2009). As discussed in Ghisellini et al. (1994), the

reflection by the inner disk also contributes to the EW by 100–150 eV (Matt et al. 1992). However, various ionization states, Doppler, and relativistic effects would smear the Fe-K line features, meaning that the Fe-K line from the inner disk is not single nor narrow.

A clear correlation between the column density and the 6.4 keV line EW indicates that the torus is an absorber with a large solid angle and that the torus column density varies within the range $10^{23-24.5}$ cm^{-2} on an object by object basis. Large EWs of 6.4 keV at $N_{\rm H} < 10^{23}$ cm^{-2} mean that the reflection material differs from the absorber. Therefore, the absorber below 10^{23} cm^{-2} is not a torus, but a low column material toward the off-torus direction. In the case of $N_{\rm H} = 10^{22}$ cm^{-2}, the low ionization state of $\xi < 1$ constrains the distance of the absorber to > 0.3 kpc for luminosity of 10^{43} erg s^{-1}. Therefore, the matter is likely to be part of the interstellar medium (Matt 2000; Guainazzi et al. 2005).

Based on the broadband X-ray spectroscopy, it has been reported that the relative reflection component for Seyfert 2 galaxies is larger than that of Seyfert 1 galaxies (Malizia et al. 2003). However, there is no trend of higher EW for larger column density below 10^{23} cm^{-2}. Above 10^{23} cm^{-2}, the correlation between the EW and column density constrains the solid angle to $(0.2-0.5)\times 4\pi$, comparing the relation obtained by the simulation (Ghisellini et al. 1994; Ikeda et al. 2009). This is not different from $(0.2-0.7)\times 4\pi$ of Seyfert 1 galaxies. Figure 11 shows the 6.4 keV line intensity ratio against the flux in 10–50 keV, which corresponds to the emission efficiency of the 6.4 keV line against the direct nuclear emission, since the observed flux in 10–50 keV is almost equivalent to the flux of the direct nuclear emission, as described in §3. Therefore, this ratio is not significantly affected by the absorption like the equivalent width and is calculated as $(4.3-7.9)\times 10^5$ erg^{-1} for the photon index of 1.5–2.2, a solid angle of $\Omega_{0.2} = 0.2\times 4\pi$, a reflector column density of 1×10^{24} cm^{-2}, Fe abundance of $A_{\rm Fe,1solar}$ =1 solar, Fe-K fluorescence yield of 0.34, and a Kα fraction of 0.88. The observed ratio is almost within the range $(2.5-7.0)\times 10^5$ erg^{-1} for various absorption column densities, suggesting that the 6.4 keV emitter has a geometrical structure with $A_{\rm Fe,1solar}\Omega_{0.2} = 0.5-1.0$ commonly for many Seyfert galaxies, and that no clear difference exists between Seyfert 1 and 2 galaxies. Some Compton-thick objects exhibit a large ratio above 10×10^5 erg^{-1}; Circinus Galaxy, NGC 1068, NGC 2273, NGC 4968, ESO 323-G032, and Swift J0601.9-8636, indicating that no direct nuclear emission is observed even above 10 keV, namely, that they are reflection-dominated. Another possibility is that the solid angle of torus is exceptionally large as suggested for Swift J0601.9-8636 (Ueda et al. 2007). The ratio of NGC 4945 is $(2.20\pm 0.15)\times 10^5$ erg^{-1} for $N_{\rm H} = 2.5\times 10^{24}$ cm $^{-2}$. When correcting the absorption, the flux becomes 1.5 times higher, and the ratio is reduced to 1.46×10^5 erg^{-1}, which is consistent with the suggestion that NGC 4945 has a small solid angle of torus (Itoh et al. 2008). This plot is therefore very useful to consider the torus solid angle and distinguish whether or not the continuum is reflection-dominated.

The relation between the absorption column density and the EW of the 6.4 keV line, together with the ratio of the Fe-K edge depth and the reflection hump around 20 keV, indicates that the Fe abundance of the reflector and absorber is around 0.7–1.3 solar. Detailed spectral modeling of the Suzaku spectrum of the Compton-thick MRK 3, based on the simulation, is almost consistent with 1 solar abundance (Ikeda et al. 2009). For the Compton-thick NGC 1068, the Fe abundance was reported to be 2–4 solar, based on detailed analysis of the neutral and ionized Fe-K lines (Matt et al. 2004; Bianchi et al. 2005). An enhanced starburst activity of NGC 1068 would cause an overabundance (Bruhweiler et al. 1991), but this is an open issue.

5.2. Properties of Ionized Material

In most cases, the EW of the ionized Fe-K emission lines is 5–50 eV. Referring to the Kα fluorescence yield $\sim$0.7 of Fe^{+25} (Krolik & Kallman 1987), the EW of the emission line due to fluorescence of the ionized material, which is not so Compton-thick, becomes $300\frac{\Omega}{4\pi}\tau_e$ eV, where $\tau_{\rm e}$ is the photoelectric optical depth of the ionized matter. Resonance scattering by the material outside the line of sight could become the dominant source of the emission line in the optical-thin regime ($\tau_{\rm e} << 1$) (Matt et al. 1994). Therefore, both fluorescence and resonance scattering contribute to the Fe-K emission lines, but the fluorescence dominates for higher column density. Bianchi and Matt (2002) calculated the EW of ionized Fe-K lines from both fluorescence and resonance scattering, and their results indicate that the observed EW of 5–50 eV requires a column density of $> 10^{21-23}$ cm^{-2}. In their geometry, the solid angle of the ionized material is $0.26 \times 4\pi$. About 30% of objects exhibit an ionized emission line at 1.5σ level (90% confidence level), indicating that the ionized material of the above column density subtends about 30% of 4π, which resembles the situation in Bianchi and Matt (2002).

On the other hand, the EW of ionized Fe-K absorption lines is often 5-40 eV. Chandra HETG observations of some Seyfert galaxies reported the width of Fe-K absorption lines to be around several 1000 km s^{-1} (Kaspi et al. 2002; Risaliti et al. 2005). According to the growth curve of the Fe-K absorption lines (Bianchi et al. 2005), the column density $N_{\rm H}$ of the absorption matter toward the line of sight is $10^{21.5-22.5}$ cm^{-2}, corresponding to $\tau_{\rm e} = 0.01 - 0.1$. which suggests that the emission and absorption lines are both due to the same matter. No Compton-thick objects exhibit absorption lines, which is attributable to the significant reduction in the direct nuclear emission transmitting the ionized material around the Fe-K lines and the domination of the reprocessed component.

The ionization parameter $\xi = \frac{L}{nR^2}$ is considered to be 10^{3-4}. Therefore, taking $L =$

10^{42-44} erg s^{-1}, the distance R from the nucleus to the ionized matter is constrained to $R < 10^{16-19}$ cm. This is consistent with a time scale showing variability of the Fe-K absorption lines of around several weeks for NGC 5548 and NGC 3227. Assuming $N_{\rm H} = 10^{22}$ cm^{-2}, the density is $n = 10^{3-6}$ cm^{-3} and while the highly ionized matter is located at the broad line region, its density is much lower and the ionization state much higher than the broad-line-emitting cloud.

Some Compton-thick objects, such as NGC 1068, NGC 4945, Circinus Galaxy, and IRAS 19254-7245, exhibit strong 6.7 and/or 7.0 keV emission lines with EW$>$ 100 eV. In these cases, the ionized material should subtend a large solid angle of $\Omega > (0.2) \times 4\pi/\tau_{\rm e}$. If the ionized matter emitting the emission line is the same as that causing the absorption line, the column density is $N_{\rm H} = 10^{21-22}$ cm^{-2} whereupon the Ω becomes comparable to or exceeds 4π in most cases. Therefore, the material emitting ionized Fe-K lines for these objects differs from that of Compton-thinner objects. Assuming column density of $N_{\rm H} = 4 \times 10^{23}$ cm^{-2} and an ionization parameter of $\xi = 10^3$, the distance from the nucleus is constrained to be $R < 2 \times 10^{16} L_{43}$ cm. In the case of NGC 4945 and Circinus Galaxy with $L \sim 10^{42}$ erg s^{-1}, R becomes $< 2 \times 10^{15}$ cm or $<$ 1 light day or 10^{2-4} of the black hole Schwarzschild radius with a mass of 10^{6-8} M$_\odot$. The maser emission for these objects indicates that the inclination of the disk is nearly edge-on. Therefore, the outer disk region appears to be somewhat vertically extended and highly photo-ionized, with nuclear emission visible through this region. These parameters resemble those of the ionized matter of Fe-K absorption lines for NGC 1365 with 10 times higher luminosity, but it exhibits a blue shift of 500–1500 km s^{-1}. The rapid increase of EW of the ionized Fe-K emission lines at $N_{\rm H} > 10^{23}$ cm^{-2} indicates that the column density of the ionized material increases alongside that of the cold material. This situation is explained by the partial photoionization of the outer disk region.

5.3. Luminosity Dependence of the Environmental Material

High luminosity AGNs are shown to systematically exhibit a smaller EW for the 6.4 keV line and also possibly for the 6.7 and 7.0 keV lines. In the sample used, high luminosity AGNs include radio-quiet quasars, narrow-line Seyfert galaxies, and broad-line radio galaxies. This trend is seen even when Seyfert 2 galaxies are excluded, which show a smaller $N_{\rm H}$ for higher luminosity (e.g. Ueda et al. 2003). These indicate that both of neutral material (torus) and ionized matter are severely irradiated by the bright nucleus and a significant portion of the material becomes fully ionized and evaporated. This trend of the 6.4 keV line for Seyfert 2 galaxies matches the deficiency of Compton-thick objects for higher luminosity. Somewhat higher Fe-K edge energy for AGNs with lower absorption column density suggests that the

inner part of torus begins to be photoionized.

Low luminosity AGNs also show a smaller EW of the 6.4 keV line, but the ionized Fe-K line is not weak. It is suggested that advection-dominated accretion flow is formed when the accretion rate is much smaller than the Eddington limit (Narayan & Yi 1994, Chiaberge et al. 2006). In this case, the torus which supplies accretion material is considered smaller, and the low-density accretion flow is photoionized.

These observational features for ionized Fe-K lines can be compared with the inner radius of dust torus against the AGN optical luminosity (Suganuma et al. 2006), where light travel time δt from the nucleus to the inner radii of the torus is proportional to the square of luminosity as $\propto L^{0.5}$. When the luminosity exceeds several 10^{44} erg s^{-1}, the inner region of the dust torus evaporates and its inner radius becomes as large as 100 light days. Also, highly ionized material, which exists at a smaller radius than the torus, is fully ionized, whereupon emission or absorption lines cannot be observed. This picture matches the tendency of lower cold absorption column density for high luminosity AGNs (e.g. Ueda et al. 2003). Furthermore the higher the luminosity of the radiation, the greater the propensity for massive outflow to occur, as observed in some high luminosity AGNs. The luminosity-dependence of these properties, regardless the black hole mass scatter by two orders of magnitude, indicates that the torus is related to the structure of the parent galaxy rather than the central black hole.

5.4. Summary

We systematically analyzed the Fe-K line features of 88 Seyfert galaxies with high-quality Suzaku data, and derived the properties of matter around the nucleus. Based on the constraint of the ionization state and the relation among EW, column density, and edge depth, neutral matter causing a 6.4 keV line and 7.1 keV edge is likely to be the torus with a solid angle of typically $(0.15 - 0.4) \times 4\pi$ and an Fe abundance of 0.7–1.3 solar for both Seyfert 1 and 2 galaxies, but certain high or low luminosity objects require a very small solid angle of torus, possibly due to the small amount of accreting material or the significant photo-ionization of the torus. No systematic difference emerges between Seyfert 1 and 2 in terms of properties. We propose a new measurement value which is useful to consider the above issues; the 6.4 keV line intensity ratio against the 10–50 keV flux. Highly ionized Fe-K lines are found for 20–30% of Seyfert galaxies. Their ionization state and EW are consistent with the picture that highly ionized matter is located at the broad line region and they exists with a much lower density than the broad-line-emitter. A large EW of He-like Fe-K lines for certain Compton-thick objects indicates the contribution of the photoionized outer disk as

viewed edge-on.

In the near future, high-resolution X-ray spectroscopy by micro calorimeter will become available, which will allow the nuclear region to be probed more precisely by an order of magnitude than by current X-ray CCD observations. Compton shoulder of the neutral Fe-K line and line width are powerful parameters to constrain the location and geometry of neutral matter. Precise measurements of the line and edge features, including satellite lines, reveal information concerning the chemical state of the matter, which thus allows us to probe the dust state. The fine structure of the ionized emission or absorption lines is also a strong tool to constrain the matter density and precisely determine the ionization state, while the line profile and center energy are important to derive information of matter velocity. Such measurements are currently performed for only a few objects by long-look Chandra HETEG observations. Disk line features can also be unambiguously tested, since their features can be separated from other Fe-K line and edge features. ASTRO-H SXS is the first to perform such measurements for many AGNs and furthermore track their time variation.

The authors wish to thank all members of the Suzaku Science Working Group, for their contributions to the instrument preparation, spacecraft operation, software development, and in-orbit calibration. This work is partly supported by Grants-in-Aid for Scientific Research by the Ministry of Education, Culture, Sports, Science and Technology of Japan (20340044).

REFERENCES

Anders, E., & Grevesse, N. 1989, Geochim. Cosmochim. Acta., 53, 197

Awaki, H. et al. 1991, PASJ, 43, 195

Awaki, H. et al. 2008, PASJ, 60, S293

Awaki, H. et al. 2009, PASJ, 61, S317

Bałucińska-Church, M., & McCammon, D. 1992, ApJ, 400, 699

Beckmann, V. et al. 2006, ApJ, 638, 642

Bianchi, S., & Matt, G. 2002, A&A, 387, 76

Bianchi, S. et al. 2005, MNRAS, 357, 599

Bianchi, S. et al. 2009, A&A, 501, 915

Bruhweiler, F. C. et al. 1991, ApJ, 379, 596

Dickey, J. M., & Lockman, F. J. 1990, ARA&A 28, 215

Chiaberge, M. et al. 2006, ApJ, 651, 728

Comastri, A. et al. 2010, ApJ, 717, 787

Elvis, M. et al. 2004, ApJ, 615, L25

Fukazawa, Y. et al. 2009, PASJ, 61, S17

Ghisellini, G. et al. 1994, MNRAS, 267, 743

Guainazzi, M. et al. 2005, A&A, 444, 119

Halpern, J. P. 1984, ApJ, 281, 90

Ikeda, S. et al. 2009, ApJ, 692, 608

Ishisaki, Y. et al. 2007, PASJ, 59, S113

Itoh, T. et al. 2008, PASJ, 60, S251

Iwasawa, K., & Taniguchi, Y. 1993, ApJ, 413, L15

Kallman, T. R. et al. 2004, ApJS, 155, 675

Kaspi, S. et al. 2002, ApJ, 574, 643

Kokubun, M. et al. 2007, PASJ, 59, S53

Koyama, K. et al. 2007, PASJ, 59, S23

Kraemer, S. B. et al. 2005, ApJ, 633, 693

Makishima, K. 1986, in The Physics of Accretion onto Compact Objects, ed. K. P. Mason, M. G. Watson, & N. E. White (Berli: Springer), 249

Malizia, A. et al. 2003, ApJ, 589, L17

Matt, G. et al. 1992, A&A, 263, 453

Matt, G. et al. 2000, A&A, 355, L31

Mitsuda, K. et al. 2007, PASJ, 59, S1 Narayan, R., & Yi, I. 1994, ApJ428, L13

Palmeri, P., et al. 2003, A&A, 410, 359

Pounds, K. A. et al. 2003, MNRAS, 345, 705

Reeves, J. N. et al. 2003, ApJ, 593, L65

Reeves, J. N. et al. 2004, ApJ, 602, 648

Reeves, J. N. et al. 2007, PASJ, 59, S301

Risaliti, G. et al. 1999, ApJ, 522, 157

Risaliti, G. et al. 2005, ApJ, 623, L93

Shirai, H. et al. 2008, PASJ, 60, S263

Suganuma, M. et al. 2006, ApJ, 639, 46

Takahashi, H. et al. 2008, PASJ, 60, S69

Takahashi, T. et al. 2007, PASJ, 59, S35

Tawa, N. et al. 2008, PASJ, 60, S11

Tueller, J. et al. 2008, ApJ, 681, 113

Turner, T. J., & Miller, L. 2009, A&AR, 17, 47

Ueda, Y. et al. 2003, ApJ, 598, 886

Ueda, Y. et al. 2007, ApJ, 664, L79

Winter, L.M. et al. 2009, ApJ, 690, 1322

Yamada, S. et al. 2009, PASJ, 61, 309

Yaqoob, T. et al. 2007, PASJ, 59, S283

Zdziarski, A. A., Johnson, W. N., Done, C., Smith, D., & McNaron-Brown, K. 1995, ApJ, 438, L63

Table 1. Suzaku results of Fe-K features of Sample AGNs.

(1) Object	(2) ObsID	(3) z	(4) $\log N_{\rm H}$	(5) $\log F_{\rm X}$,$\log L_{\rm X}$	(6) E_{64} (eV)	(7) $\sigma_{E,64}$ (eV)	(8) I_{64}	(9) EW_{64} (eV)	(10) EW_{67} (eV)	(11) EW_{70} (eV)	(12) $\tau_{\rm edge}$	(13) $E_{\rm edge}$ (keV)
1H0419-577	702041010	0.104	···	1.50,4.94	6364^{+39}_{-44}	< 132	4.5± 1.8	20± 8	···	···	0.12±0.03	7.40±0.26
3C33	702059010	0.060	3.74(0.04)	1.37,4.29	6395^{+15}_{-15}	< 55	8.2± 1.5	170± 32	···	···	0.63±0.10	7.11±0.14
3C105	702074010	0.089	3.61(0.16)	1.21,4.48	6434^{+33}_{-40}	< 108	7.5± 2.7	183± 65	···	···	0.47±0.15	···
3C120	700001030	0.033	···	1.83,4.23	6366^{+23}_{-24}	97^{+34}_{-30}	24.5± 4.7	50± 10	7± 4	···	0.12±0.03	7.20±0.27
3C273	702070010	0.158	< 0.47	2.27,6.09	···	···	···	< 9	6± 3	6± 3	···	···
3C382	702125010	0.058	···	1.75,4.65	6415^{+20}_{-21}	88^{+28}_{-26}	16.1± 2.9	34± 6	···	···	0.16±0.02	7.21±0.15
3C390.3	701060010	0.056	···	1.80,4.67	6413^{+20}_{-19}	84^{+28}_{-27}	17.1± 3.0	44± 8	6± 3	···	0.17±0.03	7.29±0.19
3C445	702056010	0.056	3.47(0.05)	1.51,4.38	6385^{+12}_{-13}	45^{+23}_{-32}	12.7± 1.9	102± 15	···	···	0.32±0.04	7.13±0.13
3C452	702073010	0.081	3.74(0.06)	1.27,4.46	6404^{+22}_{-21}	< 77	6.8± 1.8	190± 49	···	···	0.55±0.15	7.11±0.28
4C+74.26	702057010	0.104	< 0.50	1.72,5.15	6384^{+35}_{-34}	< 134	13.5± 4.3	39± 13	···	-14± 5	0.28±0.04	7.30±0.16
ARK120	702014010	0.033	···	1.66,4.05	6391^{+14}_{-15}	72^{+25}_{-23}	22.3± 3.2	69± 10	8± 4	···	0.30±0.03	7.11±0.10
ARK564	702117010	0.025	···	1.16,3.30	···	···	···	< 22	···	···	0.12±0.05	···
Centaurus_A	100005010	0.002†	3.15(0.02)	2.78,2.02	6399^{+3}_{-3}	32^{+6}_{-7}	242.7±10.3	76± 3	2± 1	···	0.15±0.01	7.13±0.06
Circinus_Galaxy	701036010	0.001†	4.01(0.01)	2.31,1.61	6406^{+1}_{-1}	33^{+2}_{-2}	333.3± 5.1	1379± 21	143± 7	71± 8	0.62±0.05	7.27±0.06
ESO263-G013	702120010	0.033	3.35(0.05)	1.27,3.67	6406^{+36}_{-41}	···	5.4± 2.7	70± 35	···	···	0.42±0.13	7.10±0.26
ESO323-G032	702119010	0.016	4.07(0.12)	0.70,2.45	6420^{+17}_{-16}	54^{+26}_{-32}	6.2± 1.3	823± 172	···	···	1.63±0.77	···
ESO506-G027	702080010	0.025	3.95(0.06)	1.43,3.58	6385^{+11}_{-11}	< 50	20.5± 3.3	467± 75	···	···	1.27±0.22	7.09±0.13
FAIRALL9	702043010	0.047	···	1.57,4.28	6384^{+7}_{-7}	42^{+15}_{-18}	25.6± 2.3	99± 9	10± 4	···	0.24±0.03	7.11±0.10
IC4329A	702113010	0.016	1.23(0.11)	2.28,4.04	6373^{+22}_{-23}	85^{+33}_{-31}	59.7±11.8	52± 10	···	···	0.18±0.03	7.41±0.21
	702113020		1.36(0.07)	2.38,4.14	6382^{+17}_{-17}	< 83	58.7±11.6	45± 9	···	···	0.19±0.03	7.18±0.14
	702113030		1.31(0.09)	2.36,4.12	6369^{+17}_{-18}	65^{+29}_{-31}	66.6±11.9	53± 9	12± 4	-7± 4	0.12±0.03	7.44±0.28
	702113040		1.25(0.11)	2.33,4.09	6377^{+18}_{-18}	67^{+27}_{-28}	66.1±12.1	59± 11	8± 5	···	0.16±0.03	7.26±0.20
	702113050		0.94(0.28)	2.20,3.96	6365^{+17}_{-11}	< 54	51.4± 9.9	69± 13	9± 6	···	0.25±0.04	7.31±0.18
IGRJ16185-5928	702123010	0.035	···	1.12,3.57	6431^{+30}_{-27}	< 87	6.2± 1.9	72± 22	···	···	0.22±0.07	···
IGRJ21247+5058	702027010	0.020	3.32(0.05)	2.22,4.18	6398^{+38}_{-39}	97^{+67}_{-46}	18.5± 5.9	21± 7	···	···	0.12±0.02	7.24±0.19
IRAS18325-5926	702118010	0.020	2.03(0.74)	1.44,3.41	6374^{+26}_{-26}	< 88	9.6± 2.9	38± 11	23± 5	···	0.21±0.04	7.12±0.19
IRAS19254-7245	701052010	0.062	4.57(0.16)	1.08,4.01	···	···	1.0± 0.6	515± 275	540±168	286±137	···	···
M81	701022010	0.000†	1.09(0.24)	1.20,0.36	···	···	5.2± 2.1	45± 18	37± 9	···	0.13±0.06	···
M106	701095010	0.002†	3.17(0.11)	1.23,1.08	6417^{+33}_{-32}	< 91	5.2± 1.9	43± 15	···	···	0.11±0.04	···
MCG+04-48-002	702081010	0.014	3.83(0.07)	1.57,3.20	6385^{+21}_{-25}	< 64	8.7± 2.7	184± 58	···	···	0.89±0.14	7.09±0.18
MCG+8-11-11	702112010	0.021	0.81(0.18)	2.06,4.04	6379^{+7}_{-7}	61^{+12}_{-12}	54.3± 4.4	77± 6	4± 3	···	0.12±0.02	7.11±0.14
MCG-5-23-16	700002010	0.009	3.51(0.04)	2.25,3.45	6390^{+7}_{-7}	68^{+11}_{-11}	80.2± 5.5	76± 5	···	4± 2	0.18±0.02	7.20±0.09
MCG-6-30-15	700007010	0.008	1.34(0.05)	1.78,2.90	6469^{+24}_{-25}	171^{+28}_{-29}	18.2± 2.7	40± 6	-12± 3	-19± 3	0.27±0.01	7.14±0.07

Table 1—Continued

(1) Object	(2) ObsID	(3) z	(4) $\log N_{\rm H}$	(5) $\log F_{\rm X}$,$\log L_{\rm X}$	(6) E_{64} (eV)	(7) $\sigma_{E,64}$ (eV)	(8) I_{64}	(9) EW_{64} (eV)	(10) EW_{67} (eV)	(11) EW_{70} (eV)	(12) $\tau_{\rm edge}$	(13) $E_{\rm edge}$ (keV)
	700007020		1.34(0.07)	1.81,2.93	6414^{+26}_{-27}	149^{+34}_{-32}	18.4± 3.2	44± 8	-12± 3	-21± 3	0.28±0.03	7.31±0.10
	700007030		1.34(0.06)	1.83,2.95	6400^{+23}_{-23}	102^{+34}_{-33}	17.3± 3.2	38± 7	-10± 3	-19± 3	0.29±0.02	7.28±0.08
MRK3	100040010	0.013	3.88(0.01)	1.95,3.56	6408^{+3}_{-3}	28^{+7}_{-10}	51.1± 2.4	454± 21	56± 8	15± 8	0.76±0.05	7.13±0.05
MRK79	702044010	0.022	0.98(0.32)	1.40,3.45	6397^{+10}_{-10}	44^{+19}_{-26}	21.6± 2.7	130± 16	15± 7	···	0.24±0.05	7.18±0.18
MRK110	702124010	0.035	···	1.52,3.98	6404^{+27}_{-26}	70^{+40}_{-38}	10.3± 2.6	44± 11	···	10± 5	0.10±0.04	···
MRK273	701050010	0.038	4.09(0.13)	0.93,3.43	6384^{+19}_{-26}	< 64	3.2± 1.1	765± 258	234±149	···	1.07±1.01	···
MRK335	701031010	0.026	···	1.29,3.48	6400^{+27}_{-25}	89^{+33}_{-31}	8.0± 1.7	49± 11	16± 5	···	0.33±0.03	7.16±0.11
MRK359	701082010	0.017	···	0.92,2.75	6380^{+22}_{-24}	81^{+33}_{-35}	6.3± 1.3	122± 25	24± 11	···	0.25±0.08	···
MRK417	702078010	0.033	3.66(0.09)	1.49,3.87	6371^{+25}_{-31}	< 88	7.4± 2.7	126± 46	···	···	0.61±0.13	7.08±0.19
MRK509	701093010	0.034	···	1.89,4.33	6411^{+31}_{-31}	< 112	29.1± 9.2	55± 17	14± 8	···	0.12±0.05	···
	701093020		···	1.91,4.34	6407^{+38}_{-40}	89^{+58}_{-62}	23.2± 7.0	42± 13	12± 6	···	0.13±0.04	···
	701093030		···	1.86,4.30	6404^{+41}_{-43}	< 170	31.7± 9.9	63± 20	21± 9	···	0.07±0.06	···
	701093040		···	1.86,4.30	6396^{+32}_{-25}	< 78	24.1± 7.4	50± 15	17± 7	···	0.10±0.05	···
MRK766	701035010	0.013	0.60(0.62)	1.26,2.84	6450^{+40}_{-41}	< 143	5.7± 2.1	42± 16	26± 8	-28± 7	0.27±0.04	7.13±0.19
	701035020		1.75(0.06)	1.28,2.85	6344^{+48}_{-44}	148^{+51}_{-69}	8.2± 2.4	59± 18	-39± 7	-29± 7	0.13±0.05	···
MRK841	701084010	0.036	···	1.44,3.93	6375^{+24}_{-25}	< 55	10.1± 3.3	65± 22	21± 10	···	0.23±0.07	7.15±0.26
	701084020		···	1.50,3.98	6326^{+57}_{-26}	184^{+15}_{-63}	10.9± 3.5	66± 21	···	···	0.21±0.07	···
MRK1073	701007020	0.023	4.37(0.32)	0.82,2.90	6408^{+47}_{-39}	< 112	3.5± 1.6	616± 287	···	···	···	···
MRK1210	702111010	0.013	3.54(0.08)	1.60,3.21	6386^{+13}_{-14}	< 70	16.2± 3.1	187± 35	-30± 15	-35± 15	0.77±0.09	7.11±0.13
MRK1239	702031010	0.020	3.66(0.11)	0.88,2.83	6425^{+45}_{-33}	< 110	3.1± 1.3	179± 72	···	···	1.61±0.39	7.15±0.20
NGC1052	702058010	0.005	3.40(0.07)	1.25,1.99	6383^{+20}_{-19}	< 78	8.8± 2.2	102± 25	···	-17± 11	0.29±0.07	7.13±0.24
NGC1068	701039010	0.004	3.99(0.02)	1.39,1.89	6413^{+9}_{-9}	61^{+14}_{-16}	52.0± 5.0	706± 68	290± 32	···	0.71±0.18	7.11±0.19
NGC1142	702079010	0.029	3.80(0.08)	1.53,3.79	6387^{+15}_{-16}	61^{+21}_{-22}	17.4± 3.1	361± 65	···	···	0.63±0.17	7.11±0.21
NGC1365	702047010	0.005†	3.01(0.11)	1.77,2.33	6419^{+18}_{-19}	137^{+17}_{-15}	15.6± 2.1	87± 12	-90± 4	-97± 4	0.28±0.03	7.11±0.10
NGC1386	702002010	0.003	4.31(0.08)	0.98,1.44	···	···	5.7± 2.0	996± 342	···	···	2.42±1.71	···
NGC2110	100024010	0.008	3.15(0.04)	2.41,3.54	6403^{+6}_{-6}	45^{+11}_{-13}	71.9± 5.3	50± 4	···	···	0.10±0.01	7.21±0.11
NGC2273	702003010	0.006	3.93(0.06)	1.02,1.94	6390^{+7}_{-8}	< 21	22.2± 2.0	1864± 168	···	···	···	···
NGC3079	803039020	0.004	4.33(0.06)	1.31,1.79	6407^{+23}_{-16}	< 67	3.9± 1.2	545± 160	···	-155±100	0.90±0.72	···
NGC3227	703022010	0.004	1.65(0.04)	2.01,2.53	6381^{+10}_{-10}	49^{+19}_{-25}	37.2± 4.3	81± 9	-24± 4	-26± 4	0.22±0.03	7.31±0.13
	703022020		1.99(0.04)	1.91,2.43	6395^{+11}_{-11}	72^{+17}_{-17}	42.2± 4.5	164± 17	···	-14± 7	0.38±0.05	7.24±0.12
	703022030		2.28(0.02)	1.90,2.42	6387^{+12}_{-12}	50^{+24}_{-37}	38.2± 5.0	113± 15	-24± 6	-32± 6	0.40±0.05	7.17±0.10
	703022040		1.06(0.47)	1.75,2.27	6394^{+9}_{-9}	44^{+17}_{-22}	37.1± 3.8	278± 28	36± 11	···	0.55±0.08	7.13±0.12
	703022050		2.38(0.02)	1.83,2.36	6395^{+13}_{-13}	< 70	34.3± 5.1	115± 17	-17± 7	-47± 7	0.32±0.05	7.11±0.14

Table 1—Continued

(1) Object	(2) ObsID	(3) z	(4) $\log N_{\rm H}$	(5) $\log F_{\rm X}$,$\log L_{\rm X}$	(6) E_{64} (eV)	(7) $\sigma_{E,64}$ (eV)	(8) I_{64}	(9) EW_{64} (eV)	(10) EW_{67} (eV)	(11) EW_{70} (eV)	(12) $\tau_{\rm edge}$	(13) $E_{\rm edge}$ (keV)
	703022060		2.31(0.03)	1.74,2.27	6400^{+8}_{-15}	< 44	31.6± 4.5	143± 20	-14± 8	-17± 8	0.40±0.06	7.20±0.13
NGC3281	703033010	0.011	3.79(0.06)	1.82,3.22	6403^{+10}_{-10}	< 60	26.8± 3.6	400± 54	-33± 21	-40± 23	1.11±0.16	7.23±0.13
NGC3393	702004010	0.013	4.00(0.10)	1.10,2.64	6407^{+32}_{-24}	< 52	4.3± 1.8	507± 214	···	···	1.47±0.88	···
NGC3516	100031010	0.009	3.26(0.04)	1.91,3.14	6401^{+4}_{-4}	58^{+7}_{-7}	53.2± 2.9	146± 8	-19± 3	-18± 3	0.36±0.02	7.27±0.06
NGC3783	701033010	0.010	1.57(0.04)	2.01,3.33	6397^{+6}_{-6}	54^{+10}_{-12}	69.2± 4.6	125± 8	-12± 3	···	0.23±0.02	7.28±0.10
NGC4051	703023010	0.002†	< -1.59	1.56,2.07	6405^{+10}_{-10}	< 59	16.2± 1.9	70± 8	···	-20± 3	0.33±0.03	7.14±0.07
	700004010		1.27(0.17)	1.32,1.84	6395^{+11}_{-11}	51^{+19}_{-21}	13.9± 1.8	133± 17	···	-29± 7	0.32±0.05	7.11±0.14
	703023020		···	1.46,1.97	6420^{+18}_{-19}	< 95	15.8± 2.9	91± 17	···	-24± 7	0.30±0.05	7.29±0.18
NGC4151	701034010	0.003†	3.39(0.02)	2.28,2.93	6392^{+2}_{-2}	35^{+4}_{-5}	166.1± 5.1	258± 8	···	-5± 3	0.38±0.02	7.14±0.04
NGC4388	800017010	0.008	3.55(0.01)	2.13,3.32	6405^{+2}_{-2}	38^{+5}_{-6}	82.5± 3.0	232± 8	-9± 3	···	0.47±0.02	7.15±0.04
NGC4395	702001010	0.001	1.63(0.14)	1.17,0.59	6382^{+36}_{-36}	< 103	4.0± 1.5	70± 27	···	···	0.19±0.08	···
NGC4507	702048010	0.012	3.78(0.02)	1.87,3.36	6405^{+3}_{-3}	39^{+7}_{-8}	53.1± 2.6	603± 29	55± 10	39± 10	0.78±0.07	7.28±0.07
NGC4593	702040010	0.009	···	1.42,2.67	6420^{+6}_{-6}	39^{+12}_{-15}	25.8± 2.1	244± 20	···	···	0.27±0.05	7.24±0.17
NGC4945	100008030	0.002†	4.40(0.02)	2.17,1.49	6409^{+4}_{-4}	39^{+9}_{-11}	32.4± 2.3	638± 45	153± 21	···	0.23±0.11	7.15±0.27
NGC4968	701005010	0.010	< 3.64	0.04,1.38	6430^{+16}_{-24}	< 68	5.6± 1.7	1798± 565	···	···	···	···
NGC4992	701080010	0.025	3.68(0.09)	1.51,3.66	6387^{+23}_{-24}	110^{+30}_{-29}	13.7± 2.7	281± 55	···	···	0.75±0.20	7.11±0.20
NGC5135	702005010	0.014	4.33(0.28)	1.10,2.71	6381^{+14}_{-15}	< 53	8.2± 2.0	1560± 382	···	···	···	···
NGC5506	701030010	0.006	2.44(0.07)	2.30,3.23	6420^{+10}_{-10}	61^{+16}_{-18}	82.3± 8.4	64± 7	14± 3	10± 3	0.21±0.02	7.24±0.10
	701030020		2.55(0.07)	2.33,3.26	6403^{+12}_{-12}	106^{+17}_{-16}	85.6± 7.9	64± 6	20± 3	9± 3	0.23±0.02	7.26±0.09
	701030030		2.69(0.14)	2.32,3.25	6386^{+11}_{-11}	79^{+16}_{-15}	74.8± 8.0	64± 7	5± 3	···	0.27±0.02	7.19±0.09
NGC5548	702042010	0.017	···	1.50,3.32	6395^{+11}_{-14}	< 32	18.3± 3.7	204± 41	···	35± 17	···	···
	702042020		1.00(0.49)	1.64,3.45	6367^{+17}_{-18}	60^{+28}_{-31}	20.6± 3.8	137± 25	···	···	0.13±0.07	···
	702042040		0.85(0.53)	1.64,3.46	6368^{+23}_{-23}	< 78	18.6± 5.2	68± 19	-14± 8	···	0.10±0.06	···
	702042050		< 0.68	1.66,3.48	6380^{+15}_{-16}	< 56	22.7± 4.8	120± 26	···	···	0.10±0.07	···
	702042060		1.05(0.32)	1.82,3.64	6393^{+37}_{-37}	< 133	18.5± 6.3	52± 18	-18± 7	···	0.07±0.06	···
	702042070		< 0.63	1.73,3.55	6363^{+15}_{-15}	< 53	24.9± 5.3	108± 23	···	···	0.10±0.07	···
	702042080		0.98(0.60)	1.60,3.42	6386^{+15}_{-16}	< 67	20.6± 4.0	157± 31	···	···	0.34±0.09	7.13±0.24
NGC5728	701079010	0.009	4.04(0.05)	1.64,2.92	6396^{+9}_{-9}	< 47	20.6± 2.5	850± 102	···	···	1.59±0.29	7.08±0.12
NGC6300	702049010	0.004	3.34(0.04)	1.83,2.31	6363^{+12}_{-12}	< 64	22.2± 2.8	84± 11	-17± 4	-27± 4	0.43±0.03	7.11±0.07
NGC7172	703030010	0.009	3.12(0.06)	2.09,3.31	6413^{+16}_{-16}	74^{+26}_{-27}	33.7± 4.9	50± 7	-13± 3	-16± 3	0.29±0.02	7.25±0.08
NGC7213	701029010	0.006	···	1.59,2.46	6402^{+8}_{-8}	< 45	20.1± 2.4	83± 10	18± 4	17± 4	0.13±0.03	7.17±0.22
NGC7314	702015010	0.005	< 2.99	1.19,1.90	6393^{+14}_{-14}	49^{+20}_{-23}	11.8± 2.0	124± 21	···	29± 9	0.10±0.06	···
NGC7582	702052010	0.005	3.53(0.11)	1.74,2.51	6409^{+19}_{-11}	< 48	22.7± 5.4	221± 52	···	···	0.57±0.14	7.20±0.23

Table 1—Continued

(1) Object	(2) ObsID	(3) z	(4) $\log N_{\rm H}$	(5) $\log F_{\rm X}$,$\log L_{\rm X}$	(6) E_{64} (eV)	(7) $\sigma_{E,64}$ (eV)	(8) I_{64}	(9) EW_{64} (eV)	(10) EW_{67} (eV)	(11) EW_{70} (eV)	(12) $\tau_{\rm edge}$	(13) $E_{\rm edge}$ (keV)
	702052020		3.69(0.07)	1.66,2.44	6385^{+16}_{-15}	< 64	23.7± 4.8	292± 59	45± 27	···	0.70±0.16	7.19±0.21
	702052030		3.79(0.05)	1.67,2.46	6412^{+13}_{-13}	< 60	18.9± 3.3	394± 69	···	···	0.72±0.19	7.23±0.22
	702052040		3.85(0.05)	1.58,2.37	6409^{+12}_{-12}	46^{+19}_{-25}	19.7± 3.1	454± 72	···	···	0.72±0.19	7.15±0.30
PDS456	701056010	0.184	···	0.62,4.58	···	···	···	< 17	···	···	···	···
PKS2356-61	801016010	0.096	3.41(0.12)	0.96,4.33	···	···	···	< 42	···	···	0.21±0.09	···
RBS1124	702114010	0.208	···	1.02,5.10	6412^{+87}_{-112}	< 199	···	< 59	···	···	0.10±0.07	···
SJ0134.1-3625⋆	703016010	0.030	4.31(0.17)	1.26,2.60	6300^{+37}_{0}	···	···	< 224	···	···	1.93±1.75	···
SJ0138.6-4001⋆	701015010	0.025	3.75(0.09)	1.57,3.72	6386^{+26}_{-28}	< 90	15.4± 4.8	222± 69	···	···	0.89±0.19	7.11±0.24
SJ0255.2-0011⋆	701013010	0.029	3.76(0.04)	1.72,3.99	6388^{+9}_{-9}	38^{+15}_{-19}	17.5± 2.3	221± 29	···	···	0.86±0.07	7.10±0.09
SJ0318.7+6828⋆	702075010	0.090	3.18(0.26)	1.01,4.32	6330^{+31}_{-30}	< 75	3.8± 1.7	52± 23	···	···	0.13±0.08	···
SJ0501.9-3239⋆	703014010	0.010	···	1.77,3.12	···	···	23.6± 5.6	72± 17	···	···	0.11±0.05	···
SJ0505.7-2348⋆	701014010	0.041	3.21(0.14)	1.51,4.10	6420^{+26}_{-18}	< 55	9.8± 2.9	57± 17	···	16± 8	0.14±0.05	···
SJ0601.9-8636⋆	701018010	0.006	3.86(0.12)	1.09,2.02	6399^{+9}_{-15}	< 47	21.6± 4.1	1254± 239	···	179±105	1.43±0.74	7.09±0.28
SJ0959.5-2258⋆	703013010	0.010	3.89(0.06)	1.52,2.86	6424^{+15}_{-15}	< 64	15.6± 3.0	270± 52	-43± 22	-50± 23	1.09±0.14	7.21±0.13
SJ1200.8+0650⋆	703009010	0.036	3.29(0.12)	1.44,3.92	6339^{+43}_{-39}	112^{+45}_{-41}	6.9± 2.3	55± 18	···	···	0.35±0.07	7.30±0.19
SJ1628.1+5145⋆	701016010	0.055	3.25(0.20)	1.60,4.44	6429^{+45}_{-110}	···	7.8± 5.1	45± 30	-33± 15	···	0.30±0.10	···
SJ2009.0-6103⋆	703015010	0.015	1.05(0.38)	1.63,2.98	6346^{+94}_{-46}	···	9.8± 4.9	44± 22	···	···	0.25±0.07	···
TON_S180	701021010	0.062	···	0.94,3.87	···	···	···	< 21	15± 9	···	0.17±0.07	···

[a]Swift/BAT sources. The name of Swift J*** is reduced to SJ***.

[b]The distance of these objects in unit of Mpc are as follows in parentheses: Centaurus_A (3.9), Circinus_Galaxy (4.2), M81 (3.6), M106 (7.9), NGC 1365 (18), NGC 4051 (17), NGC 4151 (20), NGC 4945 (4.3).

Note. — (4): Logarithmic absorption Hydrogen column density at the rest frame of the object in unit of 10^{20} cm^{-2}. Errors in parentheses represent the relative error. (5): Logarithmic observed flux in 10–50 keV in unit of 10^{-12} erg cm^{-2} s^{-1}, and logarithmic X-ray luminosity in 15–50 keV in unit of 10^{40} erg s^{-1}. (6)–(8): Center energy, width, and intensity of the 6.4 keV line. The intensity is in unit of 10^{-6} ph cm^{-2} s^{-1}. (9)–(11): Equivalent width of the 6.4, 6.7, and 7.0 keV lines. Negative values represent the absorption line. (12)–(13): Depth and energy of the Fe-K edge.

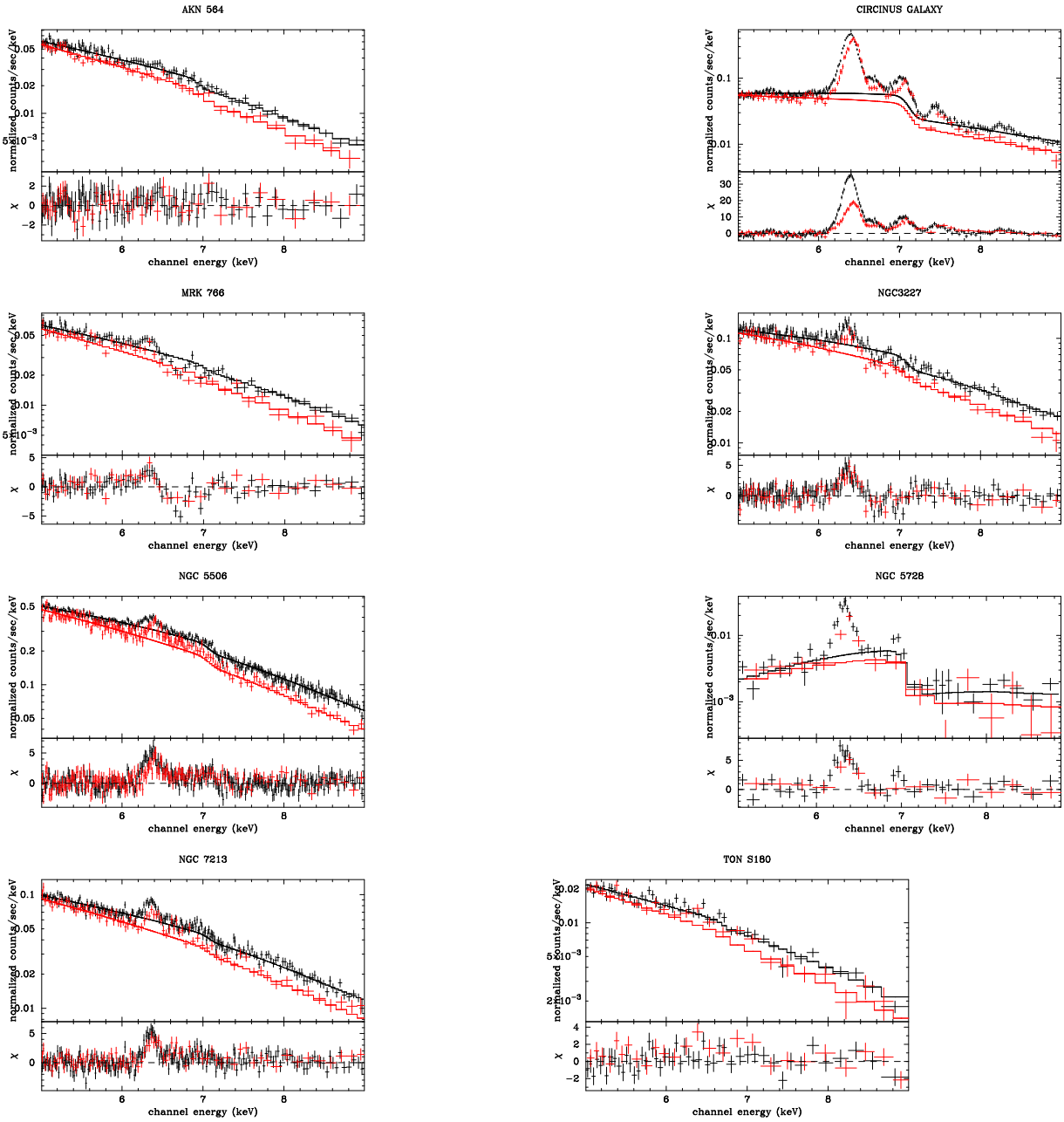

Fig. 1.— Example of the XIS spectra around the Fe-K features. From top to bottom: ARK 564, CIRCINUS GALAXY, MRK 766 (701035020), NGC 3227 (703022030), NGC 5506 (701030010), NGC 5728, NGC 7213, TON S180. The solid line in the top panel is the best-fit continuum model. The bottom panel shows the residual. Black and Red correspond to the XIS-F and XIS-B, respectively.

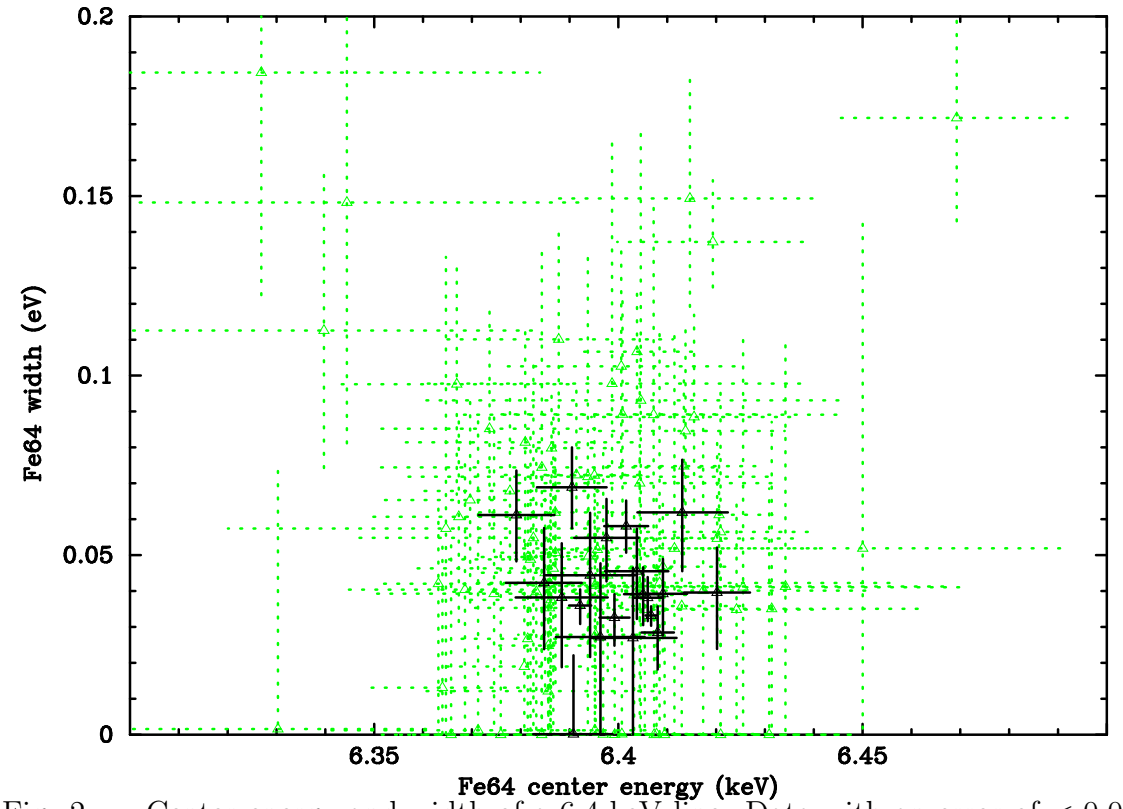

Fig. 2.— Center energy and width of a 6.4 keV line. Data with an error of < 0.01 keV for the line energy are denoted as solid error bars.

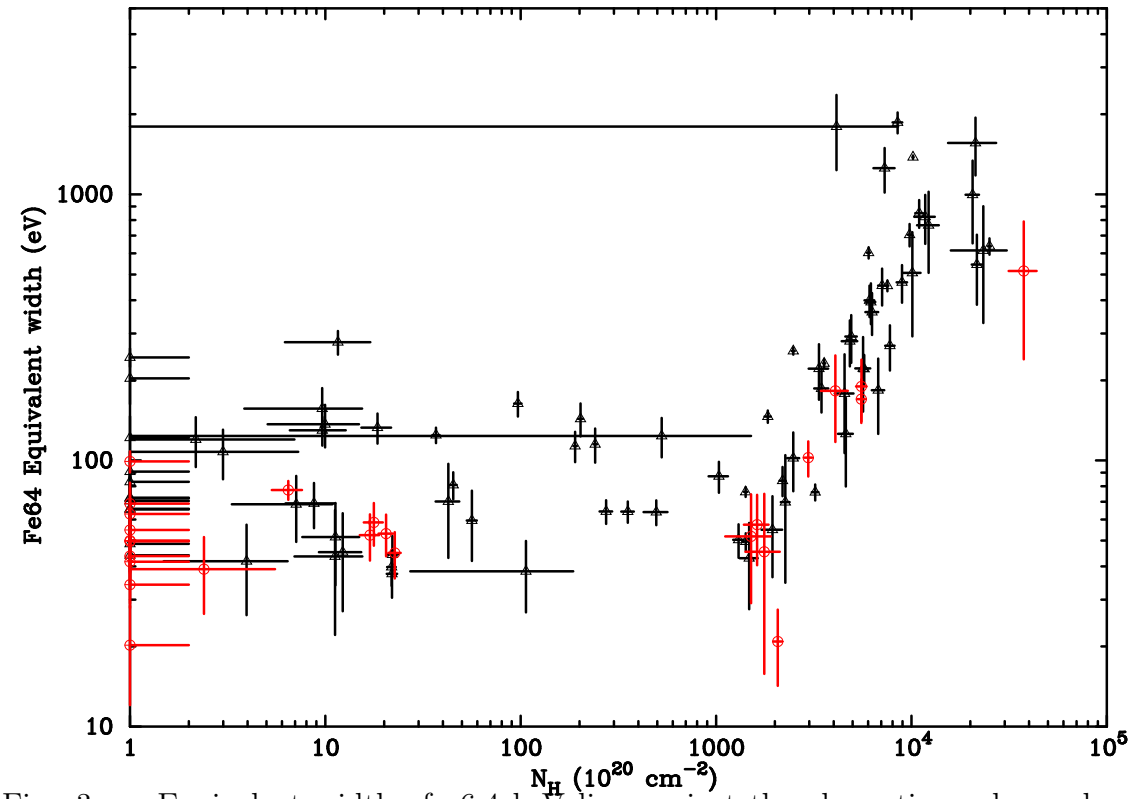

Fig. 3.— Equivalent width of a6.4 keV line against the absorption column density. Triangles (black) or circles (red) are AGNs with the luminosity of $< 10^{44}$ and $> 10^{44}$ erg s^{-1}, respectively.

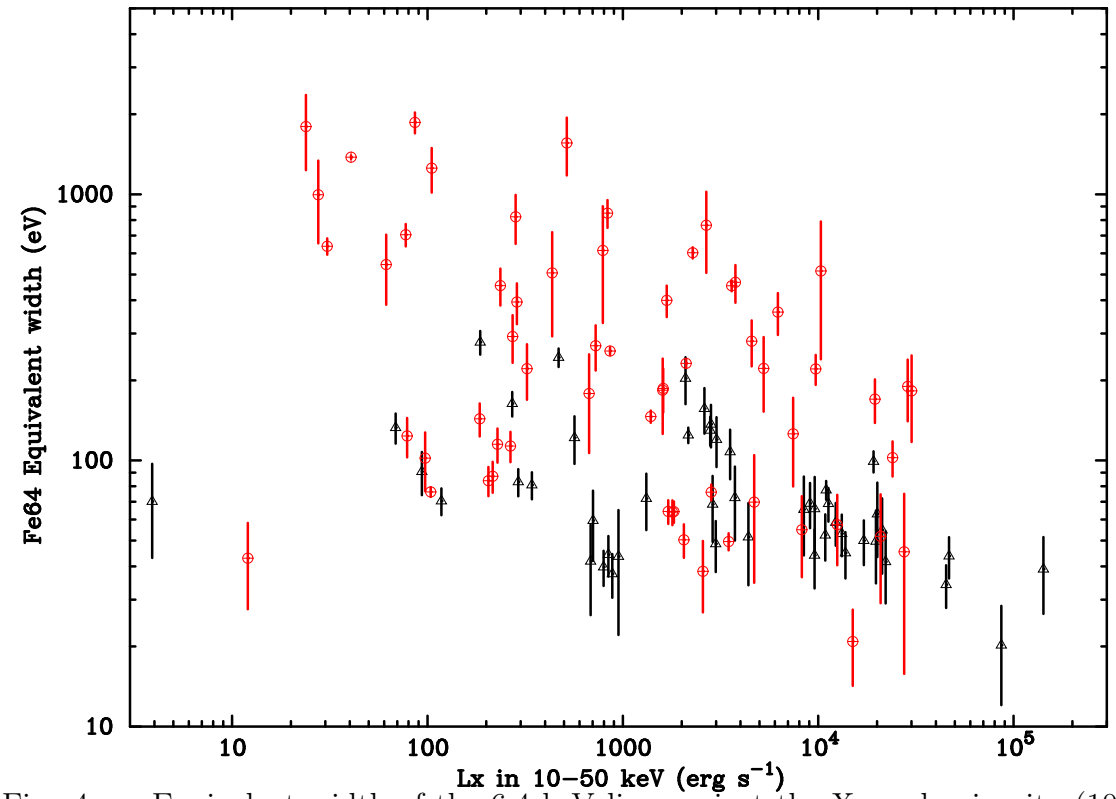

Fig. 4.— Equivalent width of the 6.4 keV line against the X-ray luminosity (10–50 keV). Triangles (black) or circles (red) are AGNs with absorption column density of $< 10^{22}$ and $> 10^{22}$ cm^{-2}, respectively.

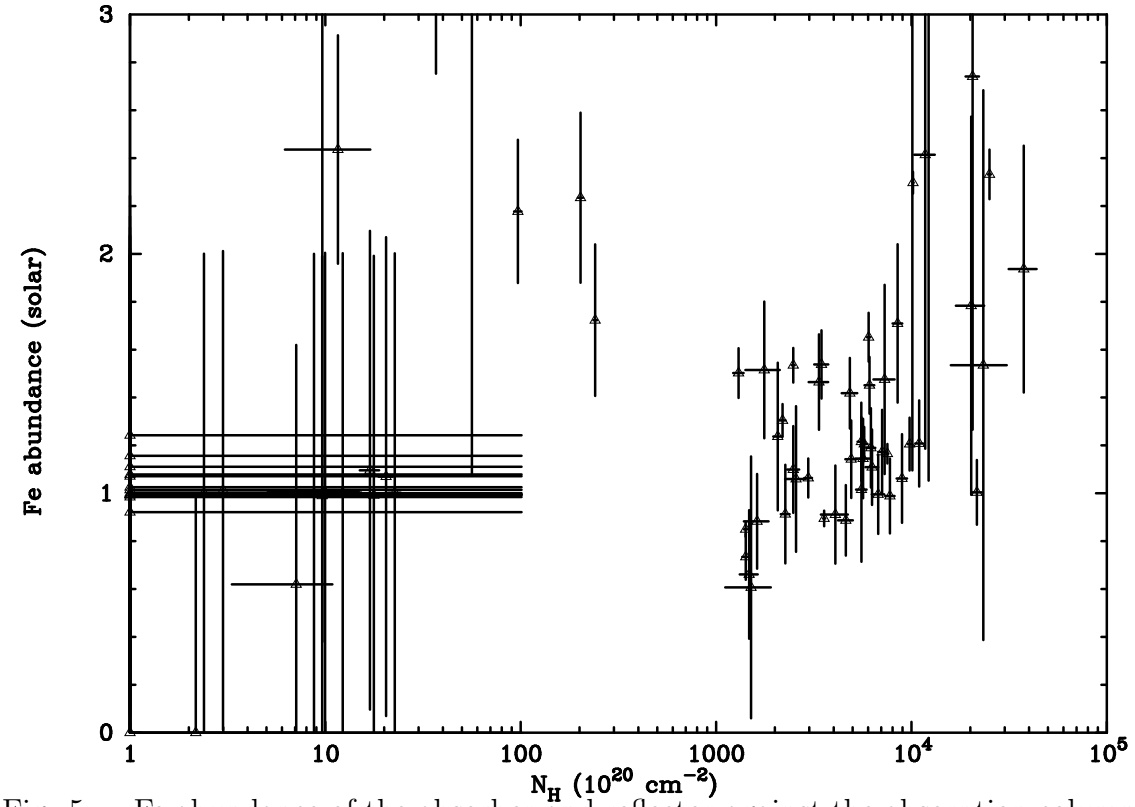

Fig. 5.— Fe abundance of the absorber and reflector against the absorption column density, derived by fitting with model A.

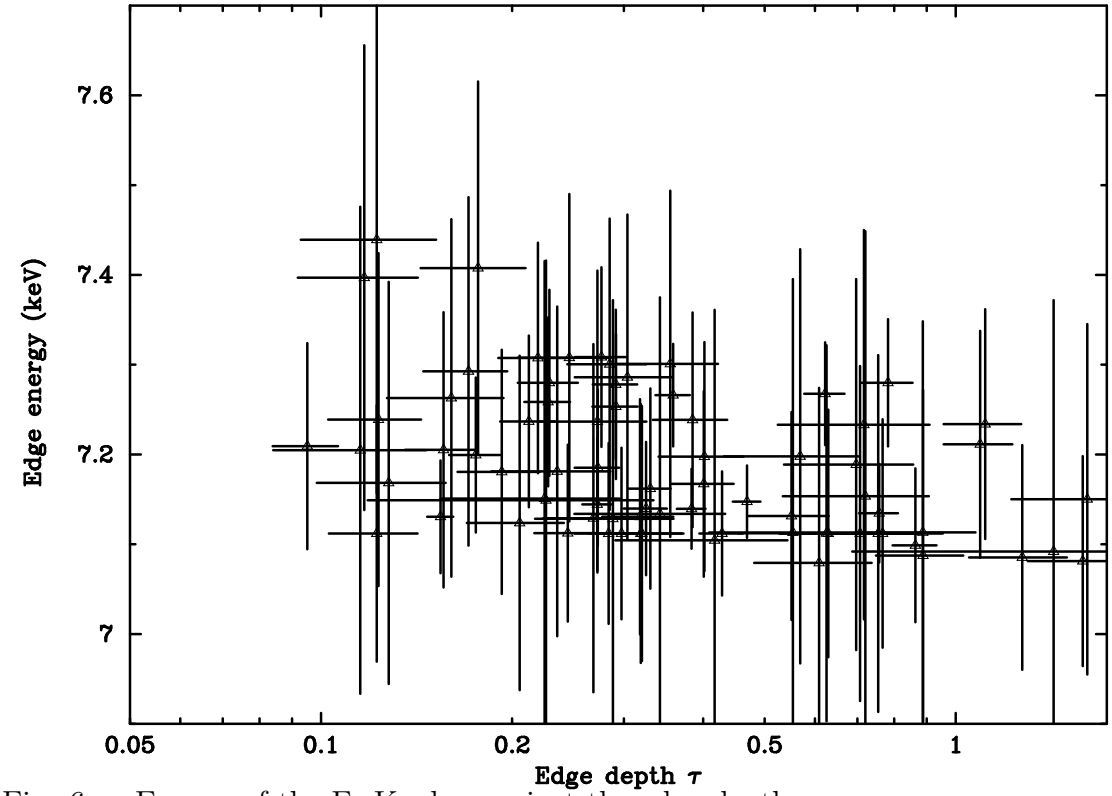

Fig. 6.— Energy of the Fe-K edge against the edge depth.

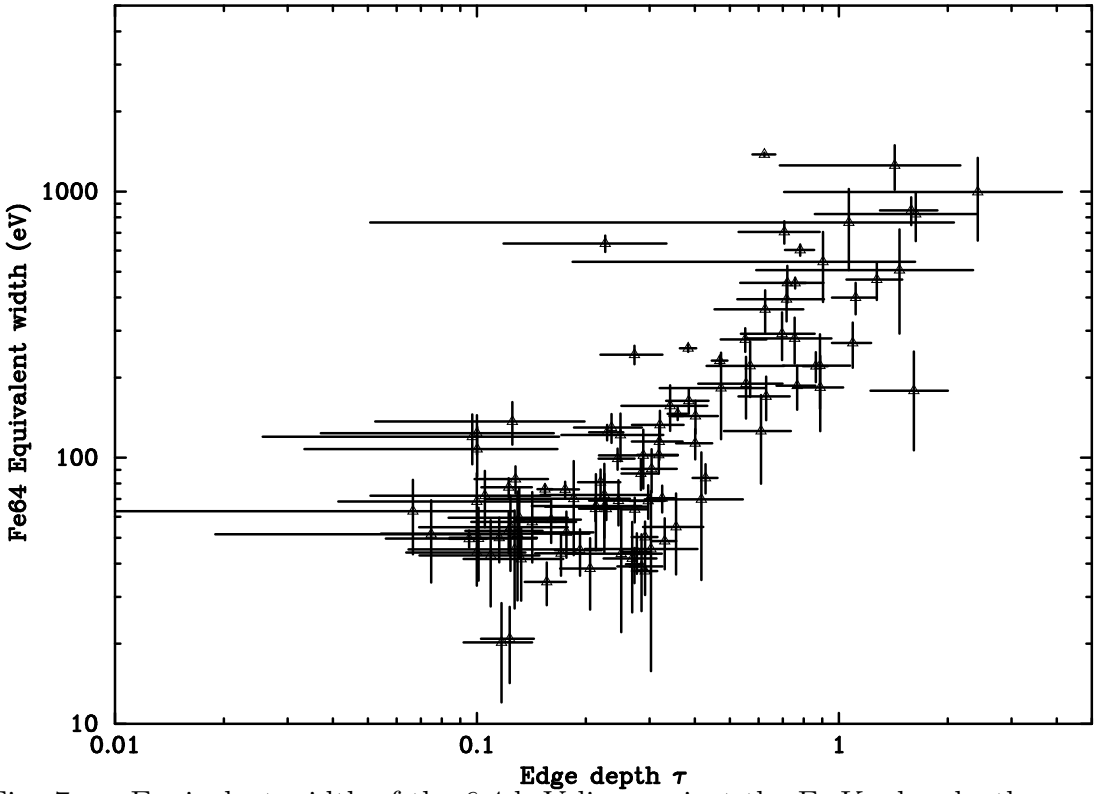

Fig. 7.— Equivalent width of the 6.4 keV line against the Fe-K edge depth.

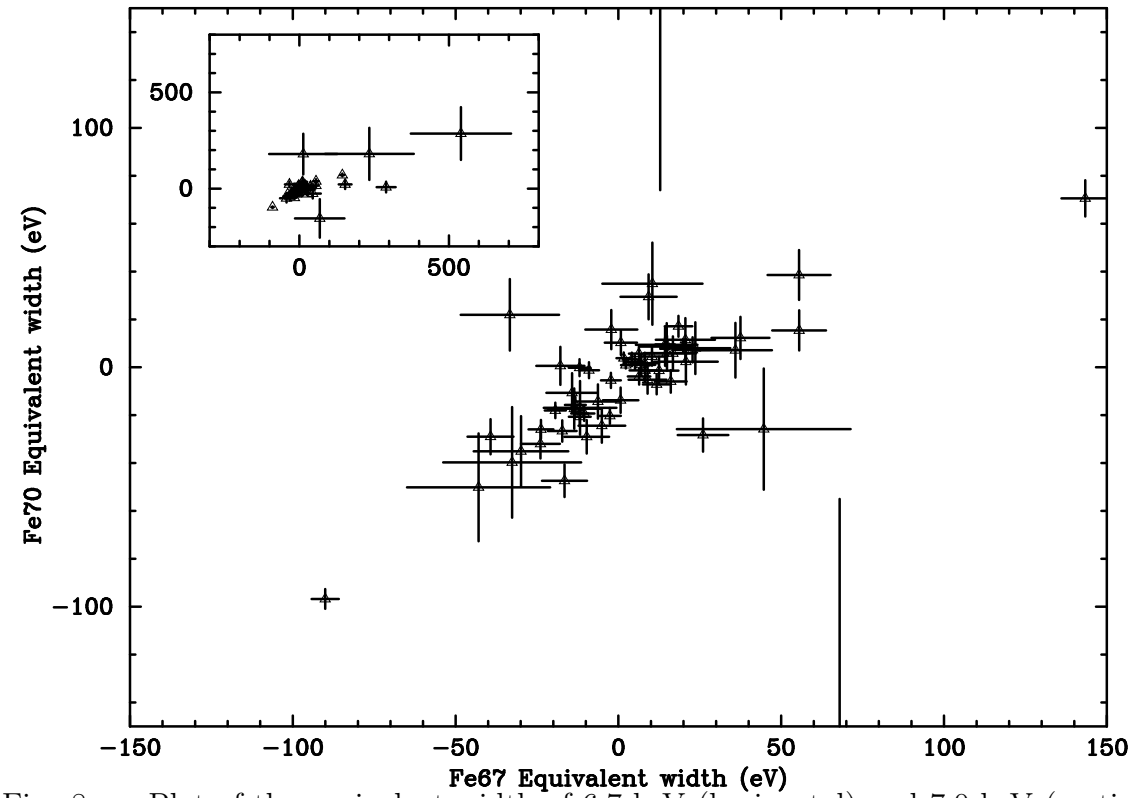

Fig. 8.— Plot of the equivalent width of 6.7 keV (horizontal) and 7.0 keV (vertical) lines. The negative values represent the absorption line. The inset is a plot where the horizontal and vertical range is enlarged.

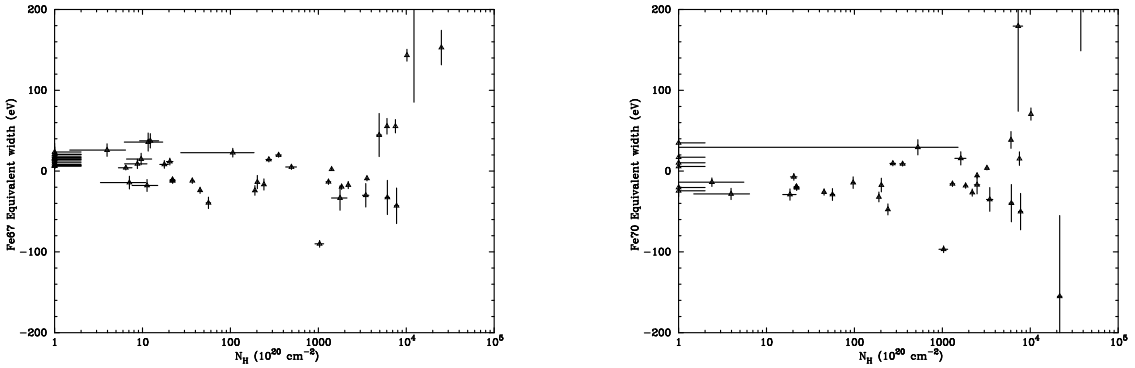

Fig. 9.— Equivalent width of 6.7 keV (left) and 7.0 keV (right) line against the absorption column density of the cold material.

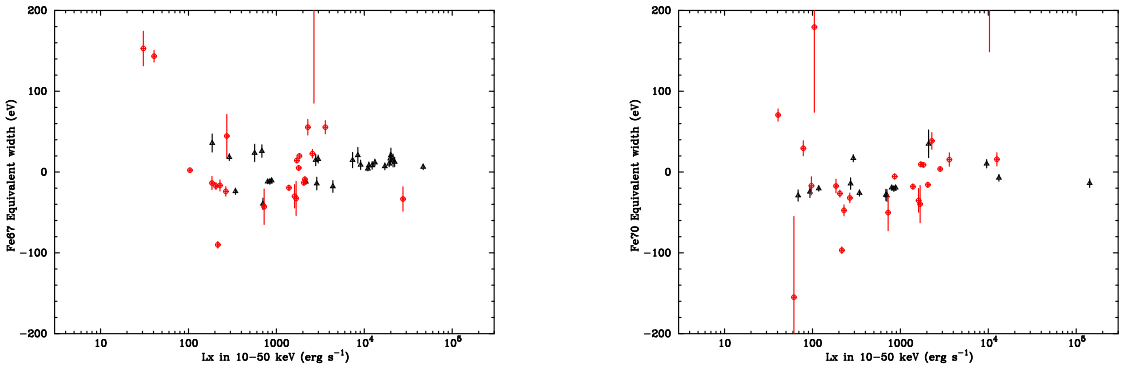

Fig. 10.— Equivalent width of 6.7 keV (left) and 7.0 keV (right) line against the X-ray luminosity (10–50 keV). Triangles (black) or circles (red) are AGNs with absorption column density of $< 10^{22}$ and $> 10^{22}$ cm^{-2}, respectively.

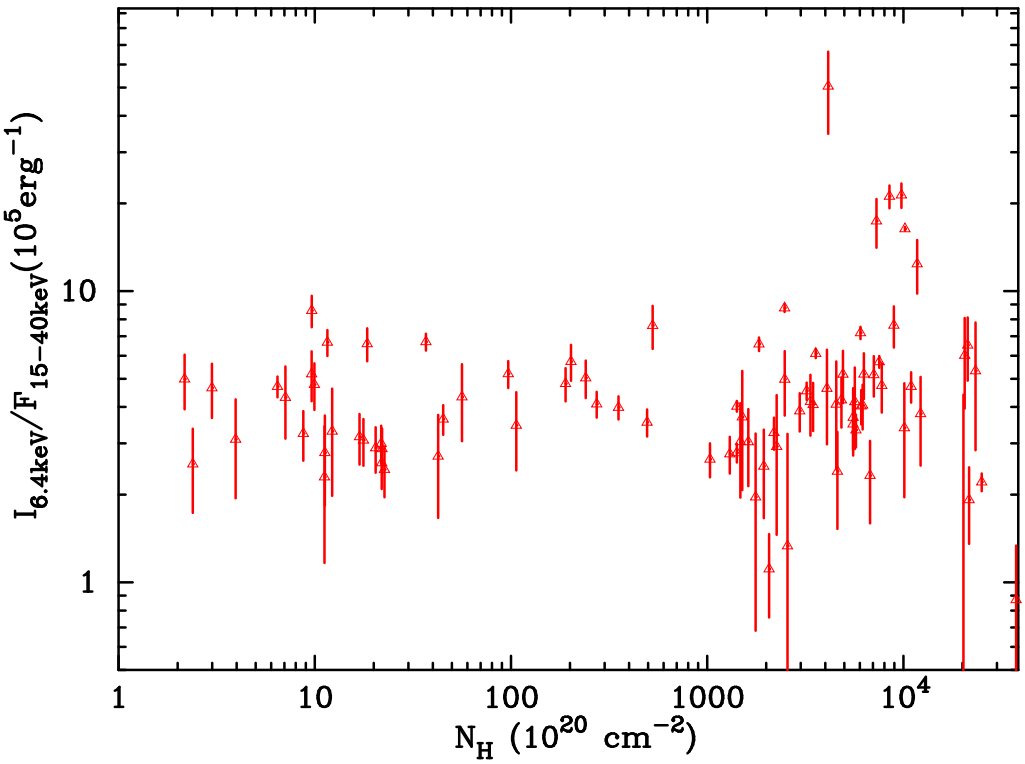

Fig. 11.— The 6.4keV line intensity ratio against the flux in 10–50 keV, plotted against the absorption column density.